CHAPTER 4

NUMERICAL INVESTIGATION

4.1 Introduction

Chapter discusses the flow characteristics near a T-shaped spur dyke situated in a reverse meandering channel with a rigid bed simulated using Renormalization Group (RNG) $k-\varepsilon$ turbulence model with an ANSYS 2018 Fluent software. To solve the model in 3D, Navier-Stroke's equation is used which is based on the principle of conservation of mass and momentum within a moving fluid. For studying the flow characteristics, Computational Fluid Dynamics was applied with all geometric parameters, and the turbulence was simulated using (RNG) $k-\varepsilon$ equations of the model. In simulation, the structured meshes are used with different diameters. To obtain accuracy in the result, the diameter of the mesh is kept high at the exit channel. This study mainly focuses on the effect of Froude number on flow pattern and several other characteristics like velocity distribution, flow separation, and bed shear stress distribution. The final result of this research work is compared with the condition where no structure is present in the channel.

The flow in a river bend or meandering channel is highly turbulent and stormy due to continuous change in curvature of banks and high topography irregularities (Pu et al., 2020, 2021). The flow pattern in a curved channel consists of spiral flow between river bed and water surface, transverse rotational flow generated by the centrifugal force in bend, secondary flow, and so on (Pandey et al., 2018a,b; Singh et al., 2019). It causes heavy bank erosion resulted in its lateral migration. Rozovski (1957), studied and

discussed the flow characteristics and boundary shear stress distribution in a curved channel. Yen (1967), experimented with flow pattern and bed configuration in a meandering channel under subcritical flow conditions. Naji et al., (2010) worked on the flow pattern in a 90° channel bend and observed that the flow in the bend is highly influenced by secondary flow and centrifugal force. They further observed that the flow near the channel orients towards the inner bank shifts to the outer bank near the water surface. Vaghefi et al., (2016) conducted an experiment at 180° channel bend and analyzed the effect of flow characteristics on bed shear stress distribution.

To prevent bank erosion in the curved channel, spur dykes are constructed across the channel width extending from the outer bank into the river. Spur dyke restricts the water flow hence, ensures deepening of the main channel. This can be used for navigation purposes, uniform discharge into an irrigation channel, and rehabilitation of flood plain. Despite its significant use, the study on spur dyke present in channel bend is still limited (Fazli et al., 2008; Vaghefi et al., 2019). The majority of studies in this field have been carried out in a straight channel such as Kothyari, and Ranga, 2001; Jennifer et al., (2011), Jiao et al., (2017); Kuhnle, and Alonso, (2013); Pourshahbaz et al., (2020); Singh et al., (2020); Xiufang et al., (2012), and so on. The flow past a spur dyke present at the channel bend or meander is highly turbulent, leading to the formation of local scour, which further increases with increasing scour depth. Therefore, it becomes essential to evaluate the flow behaviour around the spur dyke. In general, the flow regime is divided into two zones, wake-up and mixing zones around a spur. The flow characteristics around spur dyke include the formation of secondary flow, vortices, down-flow, and flow turbulence. The current experimental and numerical studies were conducted on spur dyke present in a channel bend (mainly 90° and 180°) or a meander to evaluate the inference of

several important parameters on local scour. These parameters include upstream Froude number, submergence ratio, the geometry of channel spur dyke, bed configuration, etc.

Giri et al., (2004) developed the 2D numerical model using a cubic-interpolated pseudo-particle (CIP) numerical technique to study the flow field and turbulence around spur dykes located in a rigid bed meandering channel. Sharma, and Mohapatra, (2012) experimented with a rigid bed sinusoidal meandering channel having trapezoidal cross-section and find the dimensions of the separation zone (length and width). This is highly influenced by the position of structure in the channel that varies from 4.0 to 22.8 times the spur dyke length; however, it remains nearly unchanged under varying discharge. The same results were also reported in spur dyke positioned in a straight channel (Yazdi et al., 2010).

Fazli et al., (2008) discussed as the spur dyke is shifted far from the entry of the bend, the depth of scouring and the intensity of the flow increased in a 90° channel bend. The separation zone of the vortex expands with an increase in the wing length of the spur dyke, and the vortex with the anti-clock direction was formed both upstream and downstream of the spur dyke. In addition, a vortex with a clockwise direction is also formed between wings of spur dyke in the channel walls downstream. For a single T-shaped spur dyke located at an angle of 75° (from the entry) in a 90° bend, the strength of secondary flow and vorticity gradually increases from the beginning of bend to maximum value at section 74°. It then decreases till the exit of the bend (Vaghefi et al., 2017). Therefore, it says that these vortices might be formed due to interaction between the longitudinal velocity component of flow and secondary flow. Salamatian et al., (2016) at 90° channel bend with three spur dykes placed in 50° consecutive angular spacing along the bend. The first spur dyke (from the entry of bend) was kept at 30°, 45°, and 60°. This

study shows that shifting the spur dykes downstream decreases the separation zone length while the width remains constant by increasing the bed shear stress.

Naji et al., (2010) prove with their experiment that SSIIM (Sediment Simulation in Intakes with Multiblock option) model can be used to simulate the flow pattern accurately in a 90° bend (without any structure). They then investigated the variation of flow velocity, which implements $k-\varepsilon$ model to solve Navier-Stokes's equations in a non-orthogonal grid (Olsen, 2018). Acharya, and Duan, (2011) implemented the FLOW-3D model to simulate the flow field around a series of three spur dykes using several turbulence models such as Renormalization Group (RNG) $k-\varepsilon$ model, standard two-equation $k-\varepsilon$ model, mixing length model, and Large Eddy Simulation (LES) model. They noticed that none of the models is accurately able to predict the turbulence properties. However, the RNG $k-\varepsilon$ modelcan predict the mean velocities and hence recommend the same. Kafle (2013), uses a 2D numerical model with CIP techniques to simulate flow field in spur dyke present at 90°channel bend. The turbulence models such as $k-\varepsilon$ model, zero equation models, and constant eddy viscosity model were implemented and compared. Vaghefi et al., (2014) deals with RNG $k-\varepsilon$ turbulence numerical model FLOW-3D to investigate how the change in Froude number influence flow pattern past a T-shaped spur dyke at a bend angle of 45^0 (measured from the entry) in a 90° bend and estimates to the Froude number increase from 0.2 to 0.6, vertical velocity component of flow increase about two times, and the distance between return flow and web wing of spur dyke increased by ten times. Radan, and Vaghefi, (2016) studied with SSIIM model simulate the submergence on flow and scour pattern around a spur dyke at 45° (from the entry) and 90° bends, proposed that with an increase in submergence of the spur dyke, the distance of vortices with a horizontal axis from structure decreases.

The distance of vortices with the vertical axis from the spur dyke decreases upstream but downstream remains unchanged. Similar work was done with the same numerical model but only at 90°. This work discussed the secondary flow strength and flow separation around attractive, vertical, and repelling T-shaped spur dykes. It was observed that the secondary flow is higher for the attractive spur dyke than repelling spur dyke. The separation zone increased with a rise in water elevation (Vaghefi et al., 2019).

Most research has been conducted in a 90° channel bend; researches including other curved channels such as 180° bend and meandering channel have been neglected. In hydraulic engineering, soft computing and numerical methods have been widely used and are successfully simulating hydraulic parameters (Samadi et al., 2015; Samadi et al., 2021). Therefore, this paper numerically investigates the flow pattern numerically in a reverse meandering channel near the spur dyke with a rigid bed under subcritical conditions. It also includes the effect of the Froude number on the flow pattern. The results are then compared with such a condition when no structure is located in the channel. A numerical investigation was carried out using ANSYS fluent software. The results include streamlines, velocity distribution, flow separation, bed shear stress distribution.

4.2 Numerical modelling

4.2.1 Equation Formation

Computational Fluid Dynamics (CFD) involves solving Navier-Stroke's equation based on the principle of conservation of mass and momentum within a moving fluid. In general, the conservation of mass and momentum in differential equation form is described by Equation (4.1) and Equation (4.2), respectively;

$$\frac{\partial \rho}{\partial t} + \nabla \cdot (\rho \, \vec{v}) = 0 \tag{4.1}$$

$$\frac{\partial}{\partial t}(\rho\vec{v}) + \nabla\cdot(\rho\,\vec{v}\,\vec{v}) = -\nabla \mathrm{p} - \nabla\cdot[\mu(\nabla\vec{v} + \nabla\vec{v}^{T})] + \rho\vec{\mathrm{g}} + \vec{\mathrm{F}} \tag{4.2}$$

Here, ρ = density of the fluid, $\vec{v}$= velocity of moving fluid at time t,p = pressure, $\vec{\mathrm{g}}$= acceleration due to gravity, $\vec{\mathrm{F}}$= body force, $\mu = \mu_o + \mu_t$ where, μ_o= viscosity of the fluid, and μ_t= turbulence viscosity. The RNG $k-\varepsilon$ model Yakhot et al., (1992); Yazdi et al., (2010), was used to determine the turbulence viscosity term in Equation (4.2). The turbulence viscosity is modeled as;

$$\mu_t = \rho C_\mu \frac{k^2}{\epsilon} \tag{4.3}$$

Where,

C_μ = 0.0845 (a constant), k and ϵ are turbulence kinetic energy, energy-dissipation rate, respectively. The $k\ and\ \varepsilon$ terms in Equation (4.3) are obtained from the following two transport equations.

$$\frac{\partial}{\partial t}(\rho k) + \nabla\cdot(\rho\,k\,\vec{v}) = \nabla\cdot\left[\left(\mu + \frac{\mu_t}{\sigma_k}\right)\nabla k\right] + \mathrm{G}_k - \rho\epsilon \tag{4.4}$$

$$\frac{\partial}{\partial t}(\rho\epsilon) + \nabla\cdot(\rho\,\epsilon\,\vec{v}) = \nabla\cdot\left[\left(\mu + \frac{\mu_t}{\sigma_\epsilon}\right)\nabla\epsilon\right] + C_{1\epsilon}\frac{\epsilon}{k}\mathrm{G}_k - C_{2\epsilon}^{*}\rho\frac{\epsilon^2}{k} \tag{4.5}$$

where

$$C_{2\epsilon}^{*} = C_{2\epsilon} + \frac{C_\mu\eta^3}{1+\beta\eta^3}\left[1 - \frac{\eta}{\eta_0}\right] \tag{4.6}$$

Here, G_k represents the production of turbulence kinetic energy given by $\mathrm{G}_k = \mu_t S^2$, $\eta = Sk/\epsilon$, S = modulus of the mean rate of strain tensor; σ_k and $\sigma_\epsilon$are the turbulent Prandtl

numbers; and C_μ, $C_{1\epsilon}$, $C_{2\epsilon}$, η_0, and β are constants. The value of constants in the RNG $k-\varepsilon$ model is listed in Table 4.1

Table 4.1 Value of constants in RNG k-ε model

C_μ	$C_{1\epsilon}$	$C_{2\epsilon}$	σ_k	σ_ϵ	η_0	β
0.0845	1.42	1.68	0.7194	0.7194	4.38	0.012

The RNG $k-\varepsilon$ model was developed using the Re-Normalizing Group method to normalize the Navier-Stokes equation to account for even small scales of fluid motion. Therefore, it makes RNG $k-\varepsilon$ model a suitable choice to model turbulence flow around the spur dyke. In this thesis, ANSYS fluent software (ANSYS, 2018) was used to simulate the flow around the spur dyke located in a reverse-meandering channel.

4.3 Computational meshing of 180° reverse bend channel

In this study, the reverse-meandering channel consisted of two consecutive bends of reverse order. These bends were connected with the straight inlet and outlet channels, each of length 4.0 m. The channel cross-section was kept prismatic with a uniform width of 1.0m and depth of 0.2m. The central radius of bends was designed as 1.0m. Since the relative curvature was 1.0m, such bend is categorized as a sharp bend. The central angle of the bend was kept 180° for the maximum deflection of flow and hence, generated full development of secondary circulation. Here two cases were considered:

(1) When no spur dyke was located in the bend;

(2) When a T-shaped spur dyke was located at the outer bank of the first bend.

For case 2, the spur dyke having a thickness of 0.01m (or 10mm) and a height of 0.20m was placed at an angle of 75° (measured from entry to the first bend). The spur dyke length and wing length were kept at 0.2m (i.e., 20% channel width). A schematic diagram for case 2 is shown in Figure 4.1. The CAD model for both cases was prepared in solid works, which then were imported in ANSYS fluent for further processing.

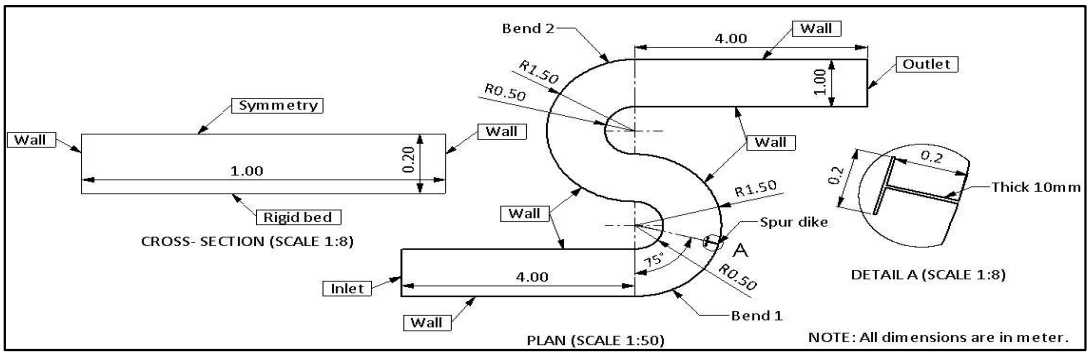

Figure 4.1 Numerical model for case 2 (i.e., spur dyke located at 75°).

By default, the unstructured mesh is available in ANSYS fluent (ANSYS 2018), and the same was used in the present research because of the complex geometry near the spur dyke. The flow simulation was iterated for several mesh configurations of progressive fine sizes to obtain the most accurate results under identical flow conditions. A mesh system was then considered, which had a negligible effect on computational results while reducing the simulation (model run) time. For case 1, uniform mesh sizes of 20mm and 40mm were used to discretize bends and inlet, and straight outlet reaches, respectively, and for case 2, a uniform mesh size of 20 mm was used in general, while a denser mesh size of 10 mm was used near the spur dyke. Some of the common parameters of volume meshing are listed in Table 4.2. The volume meshing for both cases is shown in Figure 4.2.

The flow velocity-inlet and pressure outlet were introduced at the entry and exit of the computational domain, respectively. The banks of the channel were defined as a wall with no-slip and standard wall roughness conditions. The empirical standard wall function Spalding, (1974) was used to estimate the effect of the wall on the flow field.

Table 4.2 Some general parameters of volume meshing used

S.No.	Parameters	Case 1: With no spur Dyke	Case 2: With spur Dyke
1	Number of Nodes	351450	829840
2	Number of mesh elements	31260	776559
3	Size of mesh elments	20-40mm	10-20mm
4	Type of mesh elements	Hexahedral	Hexahedral with few tetrahedral
5	Average mesh quality	0.9663	0.7131
6	Size function	Curvature	Proximity and curvature

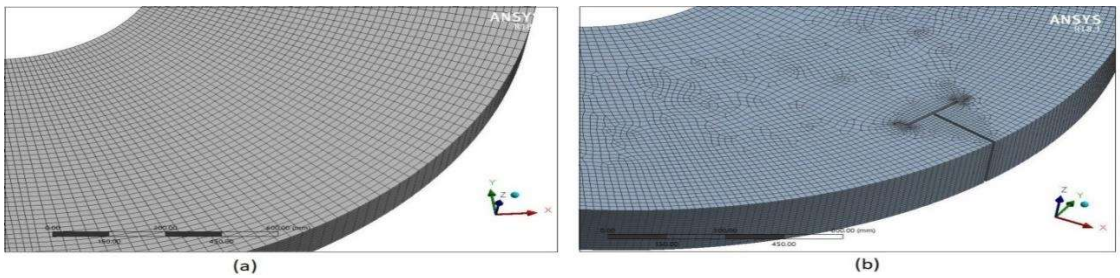

Figure 4.2 Computational mesh grid for (a) case 1: Without spur dyke, and (b) case 2: with spur dyke

The channel bed was rigid, and hence, treated as a wall. At the same time, the water surface exposed to the environment above was assumed to be symmetrical, which

enforces zero normal flow velocity and shear stress. The boundary conditions for computation are shown in Figure 4.1(marked in rectangular box). To solve the numerical model, a pressure-velocity coupling-based SIMPLE scheme was implemented. SIMPLE scheme stands for Semi-Implicit Method for Pressure Linked Equations, which uses the relationship between pressure and velocity corrections to obtain pressure field and to enforce the law of conservation of mass (ANSYS, 2018). A steady-state simulation was performed for each case with five different approaching flow conditions, i.e., Froude number equals 0.29, 0.43, 0.57, 0.71, and 0.86 (subcritical flow condition).

- **Grid dependency test for Froude no. 0.29**

To ensure the outcome of present numerical model independent of variation of grid element, a grid independency study was performed which is listed in below table 4.3.

Table:4.3 Values of Grid dependency test

S.N.	Number of mesh elements	Maximum bed shear stress at the convex tips of (N/m2) without spur dyke for first bend	% Difference for first bend
1.	24456	0.836	
2.	29453	0.852	1.92
3.	31260	0.856	0.46
4.	35789	0.858	0.24

from the above table it is found that when no. of element changes 24456 to 29453, 29453 to 31260 and 31260 to 35789 the percentage variation in maximum bed shear stress at convex tips without spur dyke for first bend is 1.92, 0.46 and 0.24 % respectively. To

optimize our computational resources, we select the optimum grid element 31260 for further studies.

4.4 Result and Discussions

4.4.1 Velocity distribution

Figure 4.3 and 4.4 shows the velocity contour at 25% and 75% water depth for case 1 (i.e., when no spur dyke is located in the bend), at Froude number equal to 0.29 and 0.86, respectively. From the figures, it is clear that the velocity distribution shows a similar trend for all Froude numbers; there is an increase in intensity and magnitude with increasing Froude number. In general, the flow velocity increases as one gradually moves from the concave side (outer bank) to the convex side (inner bank). The local maximum velocity occurs at the convex tips in both bends. Due to secondary flow formation, the lateral velocity component (across channel width) contributes significantly to the maximum velocity. However, secondary flow strength is relatively higher in the second bend due to a change in curvature of bank and flow direction as the flow enters the second bend. Hence, the maximum velocity at the convex tip of the second bend is greater than that of the first bend. The velocity streamlines are shown in Figure 4.5. In the vertical direction, the velocity increases from channel bed to water surface. In the presence of spur dyke (case 2), the velocity distribution shows significant changes, which become more prominent with increasing froude number. Similar to case 1, the flow velocity increases from the inner bank to the outer bank in both the bends, as shown in Figure 4.6 and 4.7. The obstruction to flow caused by the spur dyke increases the mean flow velocity, extending downstream from its location due to channel width contraction. Similar to case 1, the local maximum velocity is found near the convex tip (inner bank) in each bend. However, the global maximum flow velocity shifts to the convex tip of the first bend.

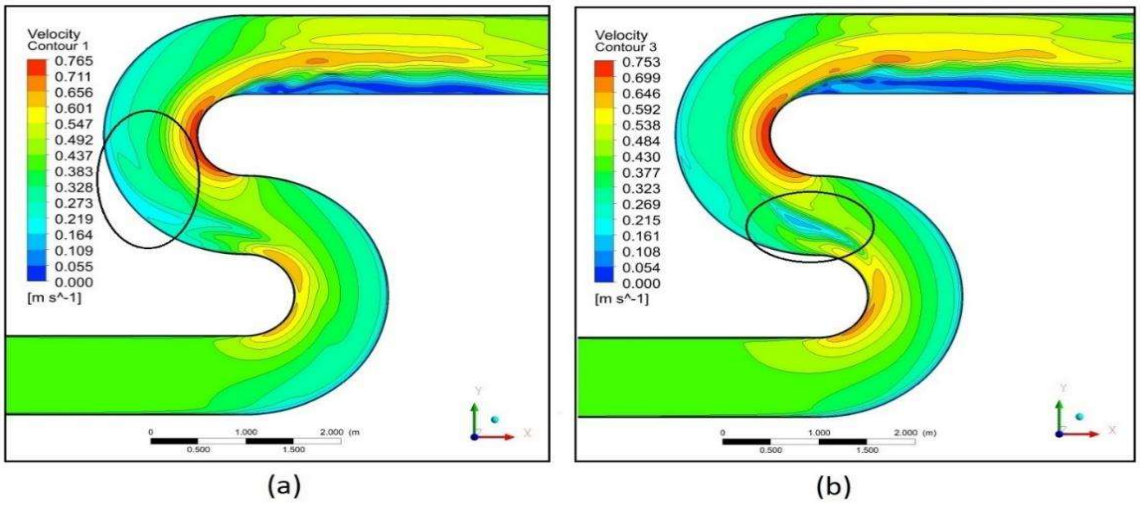

Figure 4.3 Velocity contour for case 1 (without spur dyke) for Froude number = 0.29 at (a) 25%; and (b) 75% of water depth

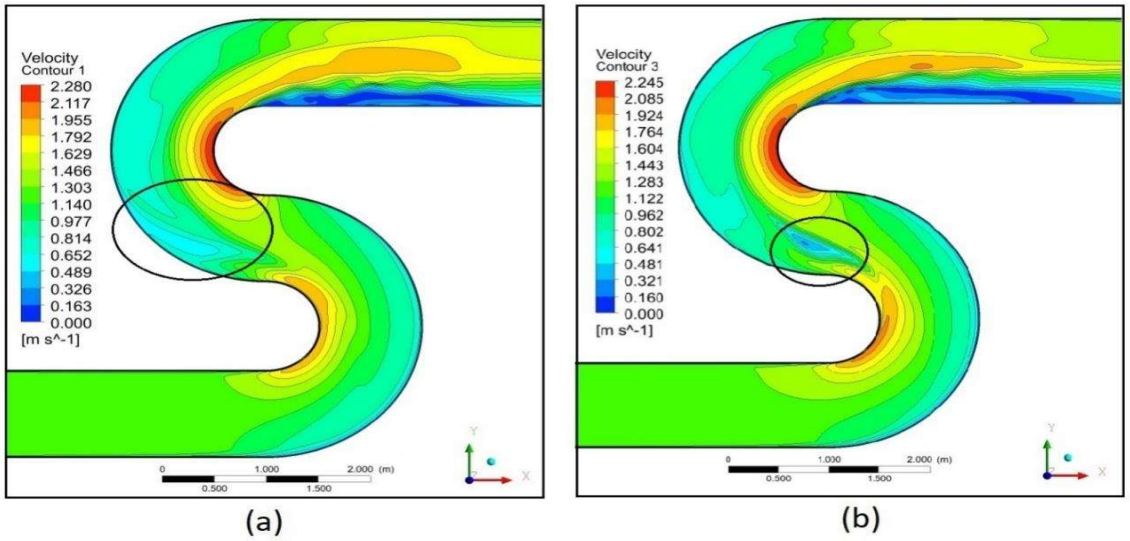

Figure 4.4 Velocity contour for case 1 (without spur dyke) for Froude number = 0.86 at (a) 25%; and (b) 75% of water depth

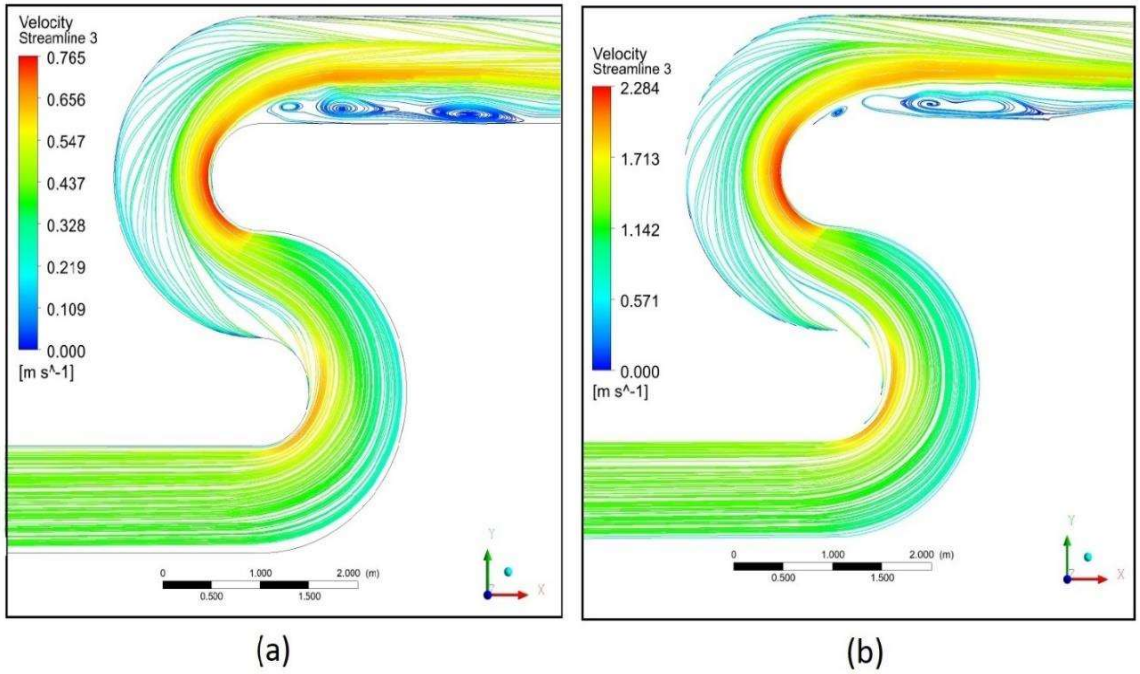

Figure 4.5 Velocity streamline for case 1 (without spur dyke) at 75% of water depth for Froude number = (a) 0.29; and (b) 0.86

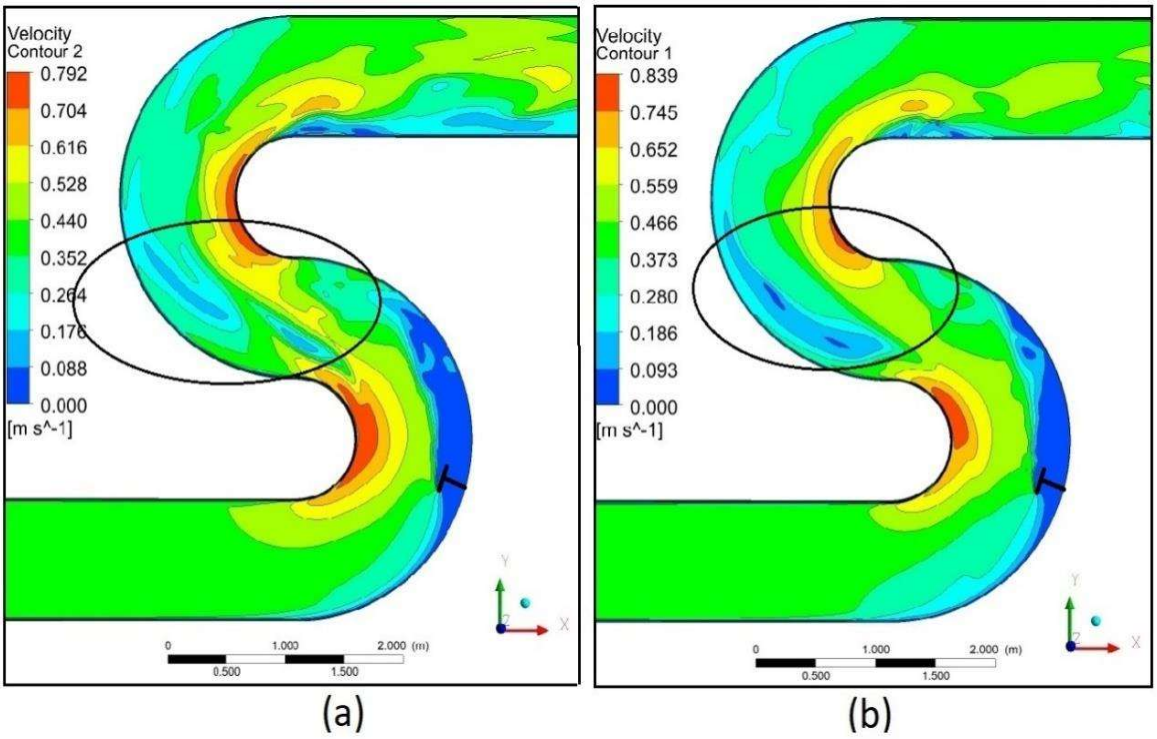

Figure 4.6 Velocity contour for case 2 (with spur dyke) for Froude number = 0.29 at (a) 25%; and (b) 75% of water depth

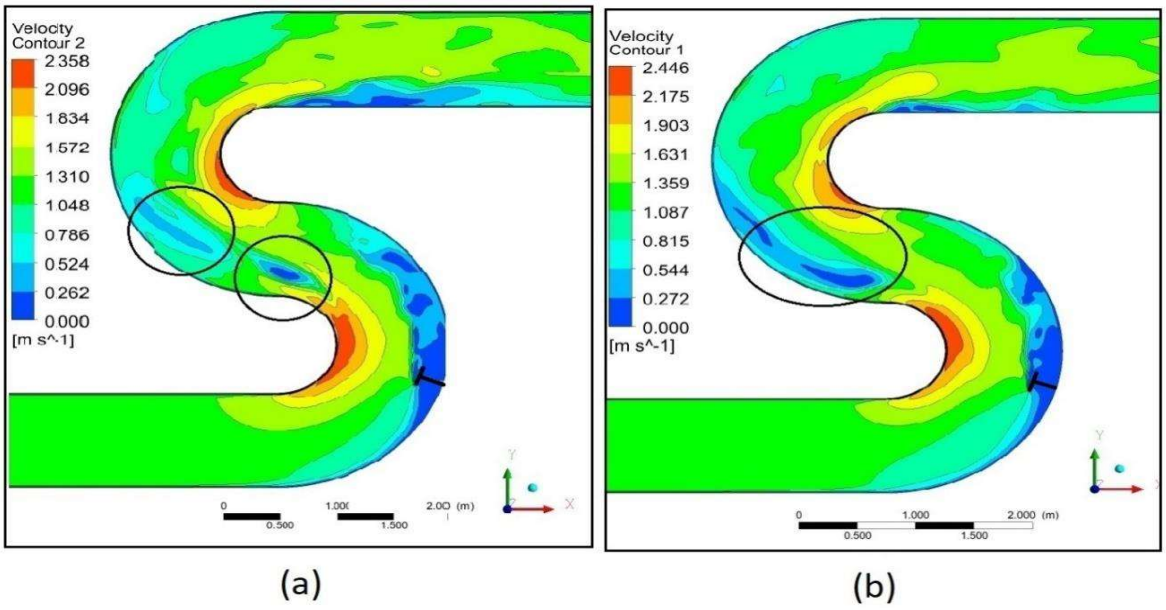

Figure 4.7 Velocity contour for case 2 (with spur dyke) for Froude number = 0.86 at (a) 25%; and (b) 75% of water depth

In the absence of the spur dyke (case 1), a low or zero velocity zone forms at the junction of two bends. The zone gets well-defined as one moves from channel bed to water surface. At a high Froude number, it becomes localized (or shrinks or converges) at the junction. Near the channel, it extends downstream along the outer bank of the second bend. It is marked with a circle in Figures 4.3 and 4.4. It occurs due to the convolution of flow reflected from the outer bank (secondary flow) and flows separation at the inner bank of the first bend shown in Figure 4.5.

In the presence of the spur dyke (case 2), there is the formation of two such low or zero velocity zones, one near the junction of two bends and the other at the outer bank of the second bend (shown in Figures 4.6 and 4.7). Similar to the previous case, these zones become well-defined near the water surface and at a higher froude number.

The 3D flow characteristics around the spur dyke (case 2) include flow, downflow, vortices, and so on, as shown in Figures 4.8 and 4.9. At location 50% of spur Dyke length

from the outer bank of the first bend, a total of three vortices having a horizontal axis of rotation are formed around the spur dyke. Two vortices with anti-clockwise direction are formed close to spur dyke, upstream and downstream, and another vortex with clockwise direction formed relatively away from spur dyke downstream. With the increase in Froud number, these vortices shift downward and show an increase in their strength as well shown in Figure 4.8(a) and 4.9(a). At the location, 100% of spur dyke length from the outer bank of the first bend (or along the wing length of spur dyke). A vortex with an anti-clockwise direction is observed at the upstream end of the spur dyke.

In contrast, several vortices are observed at their downstream end. A vortex with a clockwise direction is formed at the mid-water depth downstream of the spur dyke, which eventually dies off at a higher froude number. However, a vortex with an anti-clockwise direction is observed near the channel bed, which shifts towards the spur dyke at a higher Froude number, probably caused due to a strong returning flow shown in Figure 4.8(b) and Figure 4.9(b).

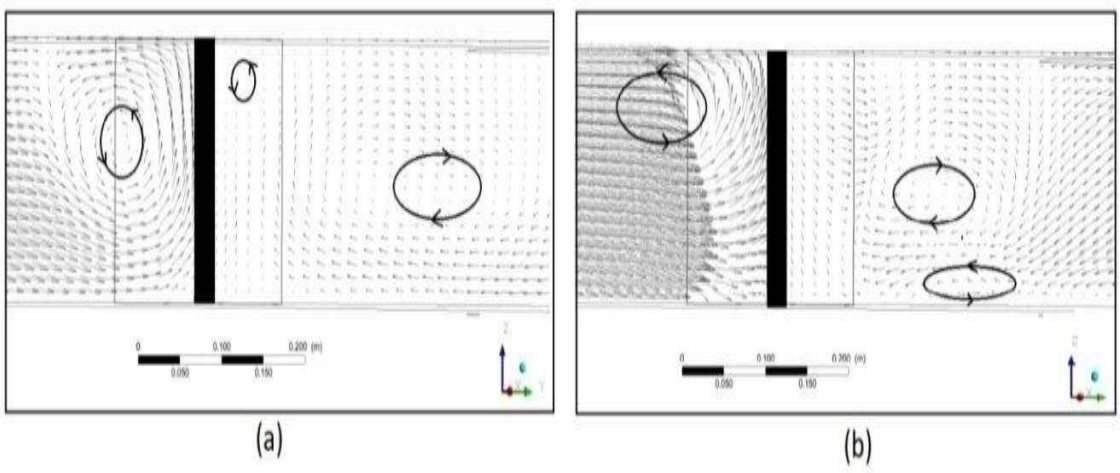

Figure 4.8 Flow velocity vector around spur dyke (case 2) for Froude number = 0.29 at location(a) 50% of spur dyke length from the outer bank of the first bend, and (b) along the spur dyke's wing (or 100%) of spur dyke length

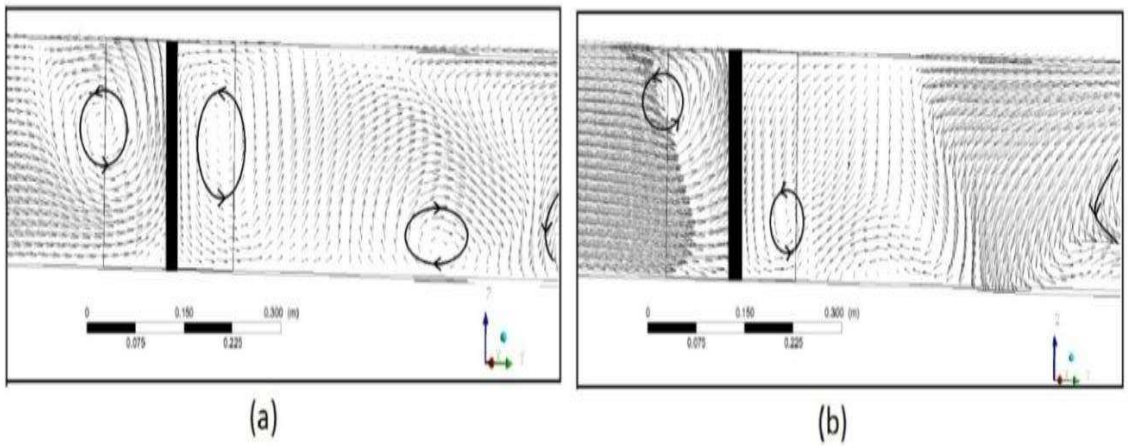

Figure 4.9 Flow velocity vector around the spur dyke (case 2) for Froude number = 0.86 at location (a) 50% of spur dyke length from the outer bank of the first bend; and (b) along the spur dyke's wing (or 100%) of spur dyke length.

4.4.2 Flow separation zone

The flow streamline starts to get separated from the boundary (i.e., channel bank) as it approaches the spur dyke. This zone is called the separation zone. The flow streamlines then reattach to the channel bank downstream, causing the formation of a reattachment zone. A schematic diagram of flow separation is shown in Figure 4.10. In the figure, separation zone and reattachment zone lengths are represented by 'm' and 'n', respectively.

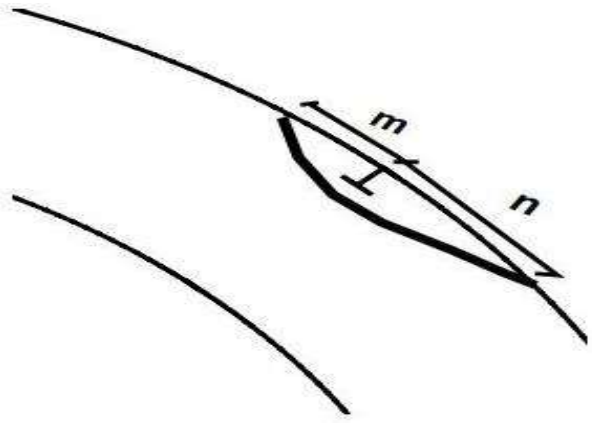

Figure 4.10 A schematic diagram of flow separation around spur dyke (adopted from Vaghefi et al., 2019)

In case 1 (absence of spur dyke), flow separation starts from the beginning of the straight outlet channel (or end of the second bend), and stretches downstream, as shown in Figure 4.3-4.5. In this case, the flow separation zone length is represented by "$m + n$." Figure 4.11 shows the variation of $(m + n)/L$ at various water depth and inflow Froude numbers. From Figure 4.11(a), it can be seen that for all values of inflow Froude number, the value of $(m + n)/L$ increases as one move towards the water surface. The value of $(m + n)/L$ is observed maximum at $\mathrm{Fr} = 0.43$, while it remains nearly unaffected at a higher Froude number shown in Figure 4.11(b). At a higher inflow Froude number, the strong secondary flow from the outer bank interacts with longitudinal flow streamlines downstream, causing the reduction in flow separation zone length.

In case 2, the flow separation in straight outlet reach becomes negligible due to reduced velocity caused by spur dyke. Table 4.3 shows the separation zone and reattachment zone length around spur dyke at two water depth levels. From the table, it is clear that the separation zone length, m/L remains unaffected by the inflow Froude number, while the reattachment zone length, n/L shows slight variation with inflow Froude number.

On comparing the values of m/L and n/L at two water depth levels, it is found out that the m/L remains nearly constant at all water depth, while n/L increases with increase as one moves from channel bed to water surface. A similar observation is made by (Vaghefi et al., 2019).

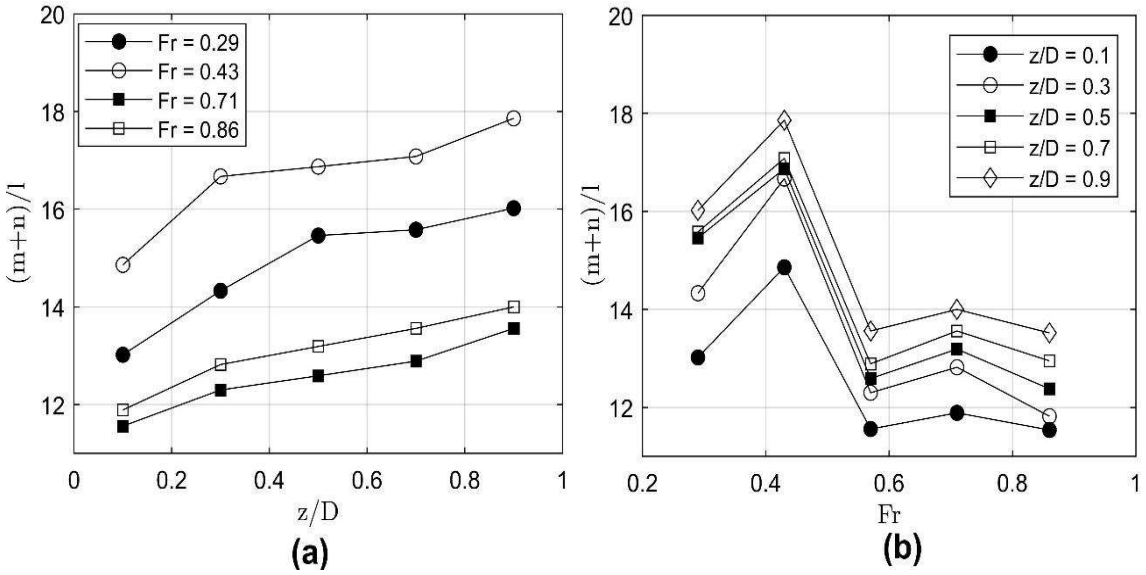

Figure 4.11 (a) (m+n)/L vs z/D; and (b) (m+n)/L vs Fr for flow separation in a straight outlet channel (Case 1)

Table 4.4 m/L and n/L values at z/D =0.25 and 0.75 for flow separation around the spur dyke (Case 2)

S.No.	Fr	$z/D = 0.25$		$z/D = 0.75$	
		m/L	n/L	m/L	n/L
1	0.29	3.28	5.32	3.42	6.37
2	0.43	3.23	5.32	3.30	6.48
3	0.57	3.17	5.31	3.28	6.34
4	0.71	3.20	5.36	3.30	6.46
5	0.86	3.26	5.36	3.36	6.47

4.4.3 Bed shear stress distribution

Even though a rigid bed is assumed in this chapter, bed shear stress distribution can provide a qualitative understanding of scouring and sediment transportation in the channel with mobile bed (or live bed condition). In general, the initiation of sediment transport at channel bed is evaluated using a critical shear-stress threshold (Ouillon, and Le, 2018). The shear-stress distribution at the channel bed gives the potential location of

sediment erosion and deposition along the channel length. The location characterized by high bed shear stress has the potential of bed erosion (or scour) or vice versa.

In case 1, the bed shear-stress distribution shows a general trend for all flow conditions. In the absence of a spur dyke, the bed-shear stress increases as one moves from the concave side (outer bank) to the convex side (inner bank). A similar observation was also made by Vaghefi et al., (2016) for a 180° channel bend. It becomes clear from Figure 4.12 that the bed shear-stress at the convex tips could potentially result in significant scour in these regions. It occurs due to high flow velocity in these regions, as shown in Figure 4.12-4.13. However, the maximum bed-shear stress occurs at the convex tip of the second bend, due to the formation of high secondary flow in the second bend which is caused by a reverse flow direction and change in curvature as water enters from bend first to second. The maximum value of bed shear stress at these two locations is listed in Table 4.5. Interestingly, the ratio of shear stress at the two locations remains nearly constant (equal to 1.38). Further, at the downstream of the second bend (i.e., the straight outlet channel), a high value of bed-shear stress is observed outside the flow separation zone, which increases drastically with an increase in Froude number, as shown in Figure 4.13.

In case 2, the bed shear-stress distribution changes drastically due to a spur dyke in the bend, as shown in Figure 4.13. However, the general trend of bed-shear remains similar to that in case 1. Due to the presence of spur dyke, the shear stress increases in both the bend. However, maximum shear stress shifts from the convex tip of the second bend to that of the first bend. In this case, the shear-stress ratio at the two locations is equal to 0.89 (a constant). The bed shear stress in the separation zone (or recirculation zone) reduces, resulting in a deposition. The same is observed at the concave side (outer bank) of the second bend. Further, the shear stress value downstream of the second bend also decreases compared to that in case 1 (shown in Figures4.12 and 4.13). Near the tip of the

spur dyke, the bed shear stress increases, resulting in bed erosion. In both cases, the shear stress increases with an increase in Froude number.

Table 4.5 Maximum value of bed shear-stress at the convex tips (side) of bends

S. No	Froude No.	Maximum bed shear stress at the convex tips of (N/m^2)			
		Case 1: Without spur Dyke		Case 2: With spur Dyke	
		first bend	second bend	first bend	second bend
1	0.29	0.856	1.183	1.389	1.235
2	0.43	1.769	2.443	2.789	2.476
3	0.57	2.968	4.108	4.613	4.111
4	0.71	4.435	6.146	6.965	6.196
5	0.86	6.160	8.525	9.472	8.415

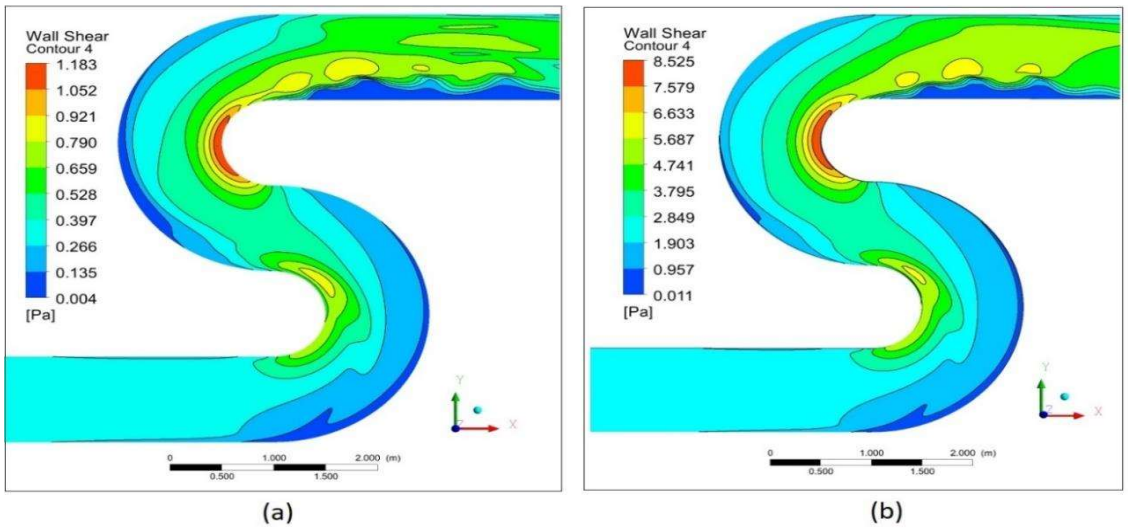

Figure 4.12 Bed shear-stress distribution in case 1 (without spur dyke) for Froude No. = (a) 0.29; (b) 0.86

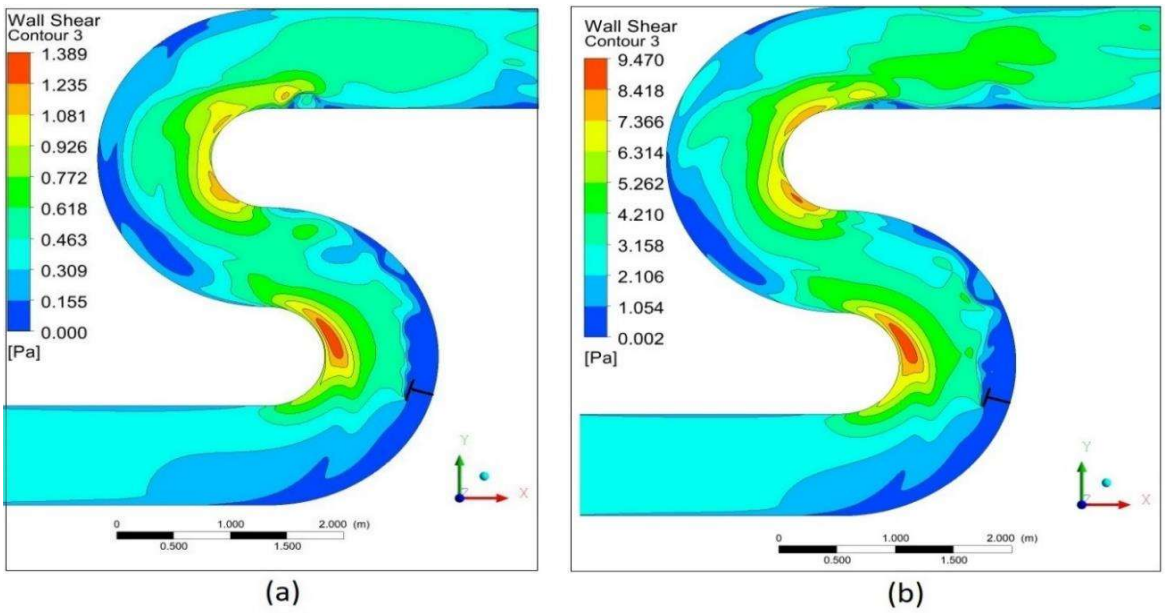

Figure 4.13 Bed shear-stress distribution in case 2 (with spur dyke) for Froude No. = (a) 0.29; (b) 0.86

4.5 Verification

For a particular numerical model to be verified, we compare the variation in the parameter of with and without spur dyke in meandering channel bend at 180-degree with the result of another experimental model under the same condition of other research paper. Present simulations are performed with five different approaching flows under the subcritical condition.

Figure 4.3 and 4.4 represents the velocity contour at 25% and 75% depth of water having Froude number 0.29, 0.86 with no structure present in the meander. This velocity shows similar trends with the Froude number. Figures 4.7and 4.8, the velocity contour with spur dyke in a meander having water depth of 75% and 0.29 Froude number, clearly shows that from the initial bend to the wings of spur dyke the velocity attended same direction and amount. It is seen that the longitudinal velocity increases at the inner wall but closer to the external bend and vertical velocity found in the mid of the meander. The direction

of velocity gets changed with the inference of spur dyke. Based on this verification, numerical modelling can be achieved.

Since no experimental investigation was carried out to study the flow pattern around a T-shaped spur dyke located in a reverse meandering channel, the experimental results validated the numerical model. Vaghefi et al., (2014) studied the inflow Froude number on flow pattern around the spur dyke located at a 45° in a 90° channel bend using RNG $k-\epsilon$ model and Volume of Fluid (VOF).

Figure 4.14 shows the comparison between experimental and numerical velocity results at a longitudinal section located at 58% of channel width and inflow Froude number equal to 0.34. From the figure, it is clear that there is a satisfactory agreement between experimental and numerical data. Hence, it validates the numerical model used in this study.

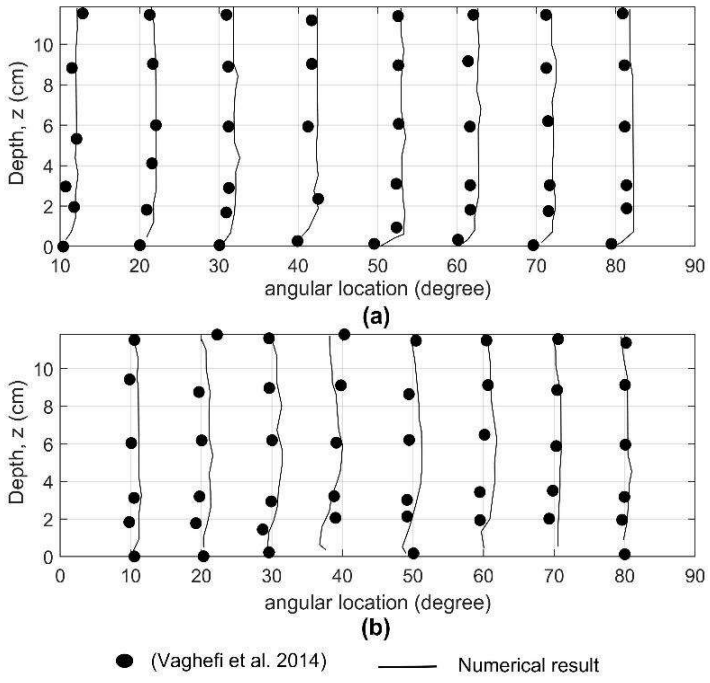

Figure 4.14 Comparison of experimental and numerical results of (a) longitudinal velocity; and (b) lateral velocity at a longitudinal section located at 58% of channel width from the outer bank of a 90° channel bend

4.6 Conclusion

The numerical simulation present in this chapter considering the parameter of with and without the spur dyke in the meandering channel has evaluated and analysed the velocity distribution, streamline, the strength of the secondary flow, bed shear stress distribution, and effect Froude number on flow. The results show that the streamline drawn in cross-section persists the two vortices in anti-clock direction and closer to the spur dyke, and these vortices shifted downwards as the strength of the stream gets increased. Since longitudinal pressure is more significant at bend surface and in the absence of spur dyke, this becomes very low. Without spur dyke in the channel, there is no formation of flow zones. Still, in contrast with spur dyke, two velocity zones are formed at the junction of two bends. Due to the spur dyke, there is a formation of secondary flow, which is maximum at the first bend of the channel. The maximum bed shear stress is formed outside the flow separation zone at the convex tip of the channel spur dyke. The meander with spur dyke becomes more complicit to protect the heavy flow in the field and helps in less damaging the river. In hydraulics, performing field experiments is very costly and almost impossible to deals with all parameters accurately within the same time. The numerical models are the best way to analyse all parameters, so we hope this numerical investigation helps in the future findings of hydraulics parameters.